Supporting Information

Cobalt Doped Black TiO_2 Nanotube Array as a Stable Anode for Oxygen Evolution and Electrochemical Wastewater Treatment

Yang Yang[a], Li Cheng Kao[b], Yuanyue Liu[c], Ke Sun[d], Hongtao Yu[e], Jinghua Guo[f,g], Sofia Ya Hsuan Liou[b], Michael R. Hoffmann[a,*]

[a] Division of Engineering and Applied Science, Linde-Robinson Laboratory, California Institute of Technology, Pasadena, California, 91125, USA

[b] Department of Geosciences, National Taiwan University, P.O. Box 13-318, Taipei 106, Taiwan

[c] Department of Mechanical Engineering and Texas Materials Institute, University of Texas at Austin, Austin, Texas, 78712, USA

[d] Divisions of Chemistry and Chemical Engineering, California Institute of Technology, Pasadena, California, 91125, USA

[e] School of Environmental Science and Technology, Dalian University of Technology, Dalian 116024, China

[f] Advanced Light Source, Lawrence Berkeley National Laboratory, Berkeley, California, 94720, USA

[g] Department of Chemistry and Biochemistry, University of California, Santa Cruz, California, 95064, USA

Corresponding Author

* Email for M. R. H.: mrh@caltech.edu.

Text S1

Density function theory calculation

The formation of oxygen vacancy enhanced by Co doping is confirmed by our spin-polarized density functional theory calculations with the LDA+U approach[1]. The calculations were performed using the Vienna Ab-initio Simulation Package (VASP)[2-3] with projector augmented wave (PAW) pseudopotentials[4-5] and The Perdew–Burke–Ernzerhof (PBE) exchange-correlation functional[6]. We use a 3x2 supercell of anatase (101) surface. The 3x3 Monkhorst-Pack k-points[7] and 400 eV plane-wave cutoff were used to fully relax the system until the final force on each atom is less than 0.01 eV/Å. U = 3.5 eV and 3.3 eV are used for Ti and Co *d* electrons, respectively[8-9] The topmost Ti and O layers of (101) plane are under coordinated, and hence are the most favorable sites for doping or defects generation. The relative formation energy (E_{rf}) of the O_v is calculated as:

$$E_{rf} = E\,(Co_{Ti} + O_v) - E\,(Co_{Ti}) - [\,E(O_v) - E_0] \qquad (1)$$

where E_0 is the energy of a pristine surface, Co_{Ti} means the surface contains Co which substitutes Ti. The E_{rf} thus characterizes the effect of Co doping on O_v formation.

Text S2

Electrochemical impedance analyses

Electrochemical impedance analyses of NTA electrodes were performed in a mixture of aqueous solutions containing 50 mmol L^{-1} $K_3Fe(CN)_6$, 350 mmol L^{-1} $K_4Fe(CN)_6$, and 1.0 mol L^{-1} KCl. The sample, a Pt mesh and a Pt wire were used as the working electrode, counter electrode and reference electrode, respectively. The frequency range used in the measurement was 30 kHz to 0.1 Hz. The solution was quiescent and was kept in the dark during the measurements without agitation. The EIS equivalent circuit model used to model the TiO_2 nanotube structure in this electrochemical environment.

$$R_u + C_d/R_{ct} \quad (2)$$

Where R_u is the solution resistance, R_{ct} is the kinetically controlled charge transfer resistance, C_d is the double layer capacitance.

The reverse-bias dependence of the area-normalized semiconductor depletion-region capacitance (C_{dl}) is given by the Mott-Schottky relation:

$$\frac{1}{C_{dl}^2} = \left(\frac{2}{A^2 q N_d \varepsilon_0 \varepsilon_r}\right)\left(\phi_b - V_n - \frac{k_b T}{q} - V_{app}\right) \quad (3)$$

where A is the area of the device, N_d is the donor impurity concentration in the semiconductor, ε_0 is the vacuum permittivity, ε_r is the relative permittivity, q is the unsigned charge on an electron, ϕ_b is the barrier height, V_n is the voltage difference between the potential of the Fermi level and the potential of the conduction-band edge of the n-type semiconductor in the bulk, k_b is Boltzmann's constant, T is the temperature in K, and V_{app} is the difference between the applied potential and the redox potential of the solution.

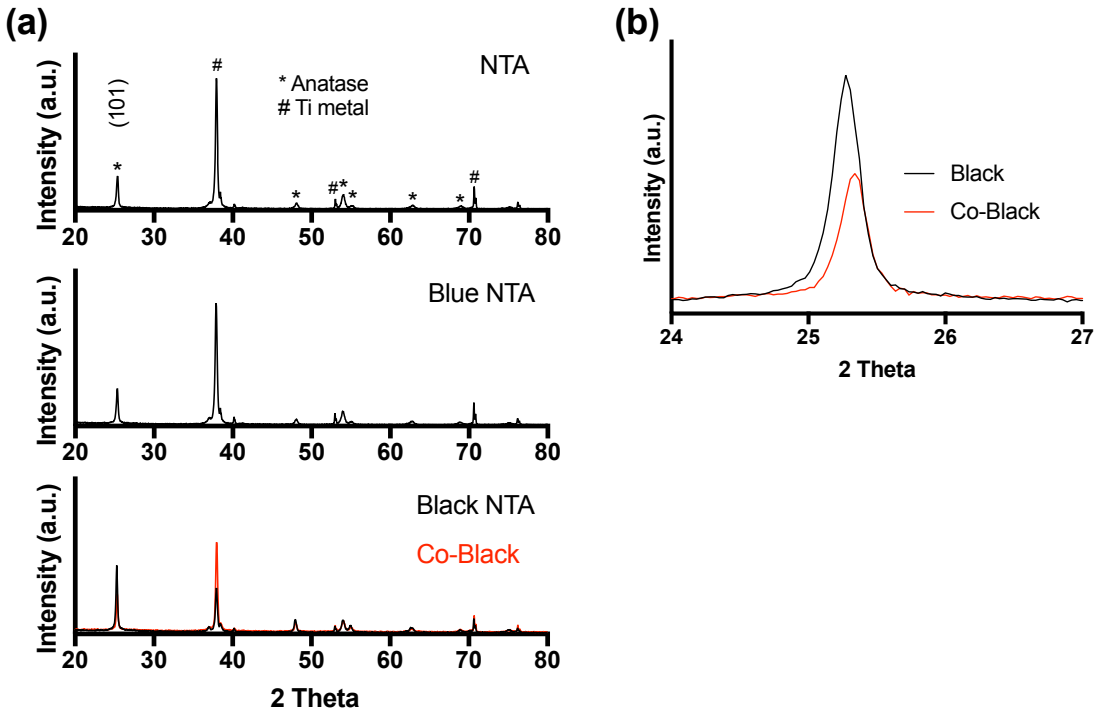

Figure S1. a) XRD of NTA electrodes. b) Enlarged XRD spectrum of (101) diffraction peaks. It is shown that pristine, blue, and black NTA are all in anatase phase with the preferential exposure of (101) plane. Cobalt doping did not affect the crystal phase, but it decreases the diffraction intensity of (101) plane.

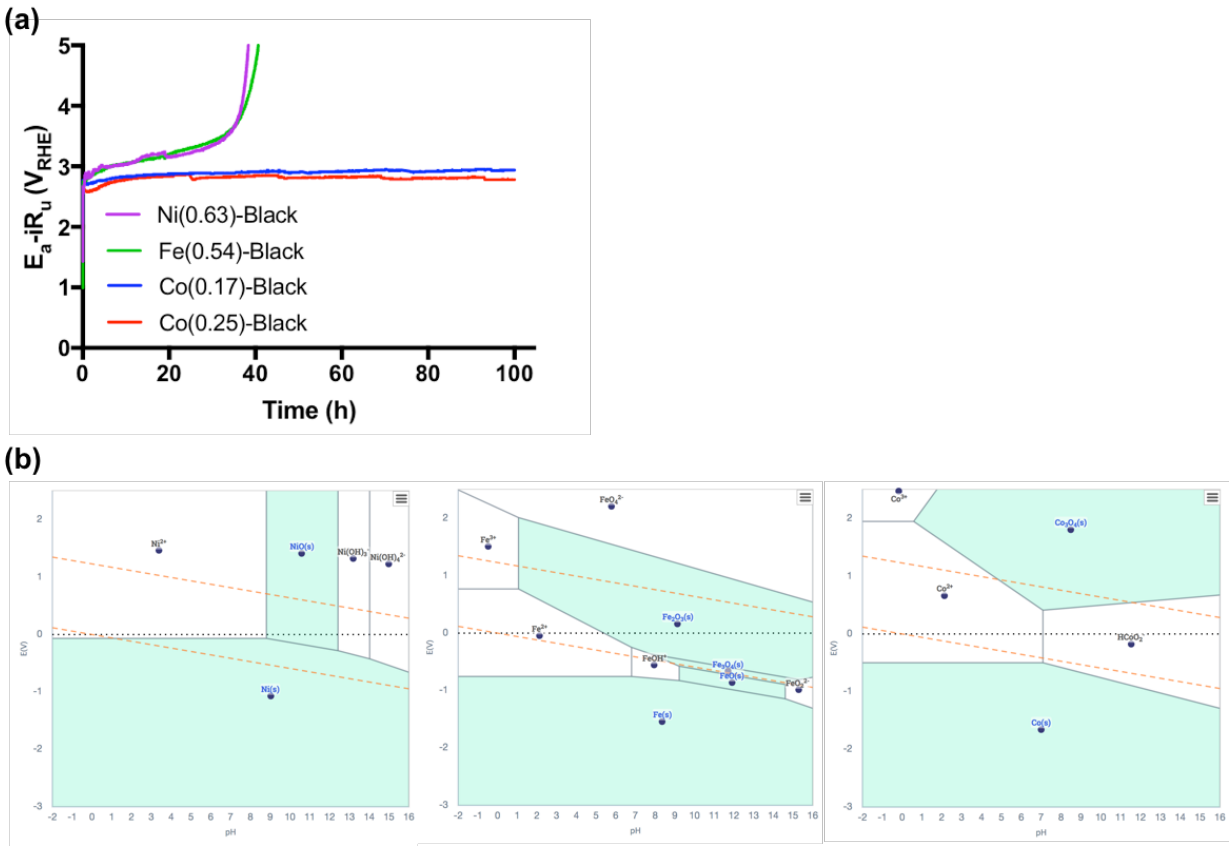

Figure S2. a) Stability tests of black NTA electrodes doped with NiO_x, FeO_x, and various amounts of CoO_x in 30 mM $KClO_4$ at 10 mA cm^{-2}. Numbers shown in the bracket are the molar loading of the corresponding element in μmol/cm^2. Dipping Amp-NTA into 250 mM $Ni(NO_3)_2$ and $Fe(NO_3)_3$ ethanol solution followed by H_2 annealing gave Ni loading of 0.63 μmol/cm^2 and Fe loading of 0.54 μmol/cm^2, respectively. b) Pourbaix diagrams of NiO_x, FeO_x, and CoO_x obtained from Materials Project (https://materialsproject.org).

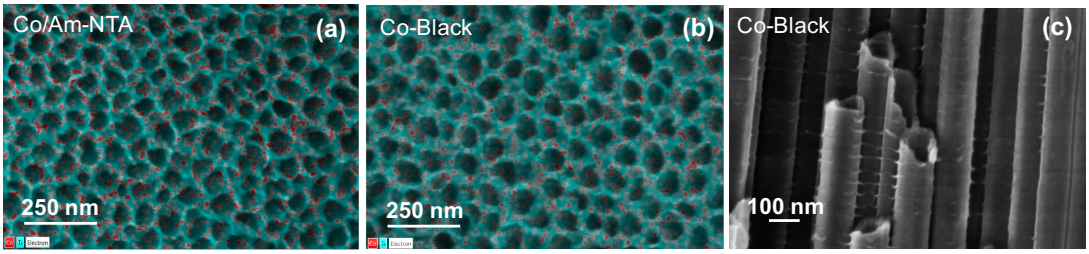

Figure S3. a & b) SEM-EDS images of NTA electrodes. in which Co rich areas are marked in red. c) Cross-section image of Co-Black shows that no particulate cobalt oxide is attached on tube wall.

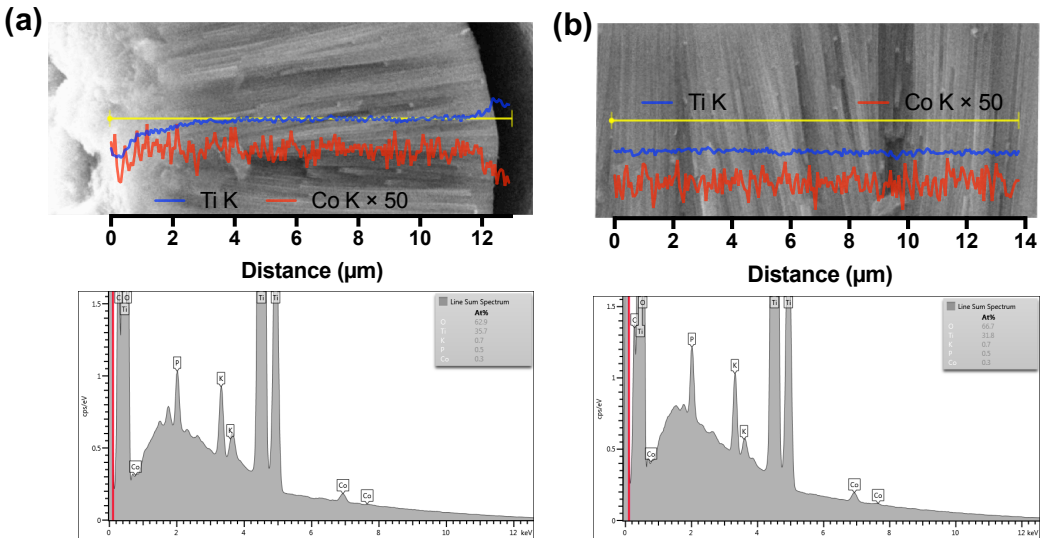

Figure S4. SEM-EDS line scan of Co-Black NTA electrode a) along with or b) perpendicular to the tube length. The lower panels show the overall EDS spectrum. Electrodes were characterized after CV analyses in KPi. Therefore, in addition to Co, K and P signals were also detected.

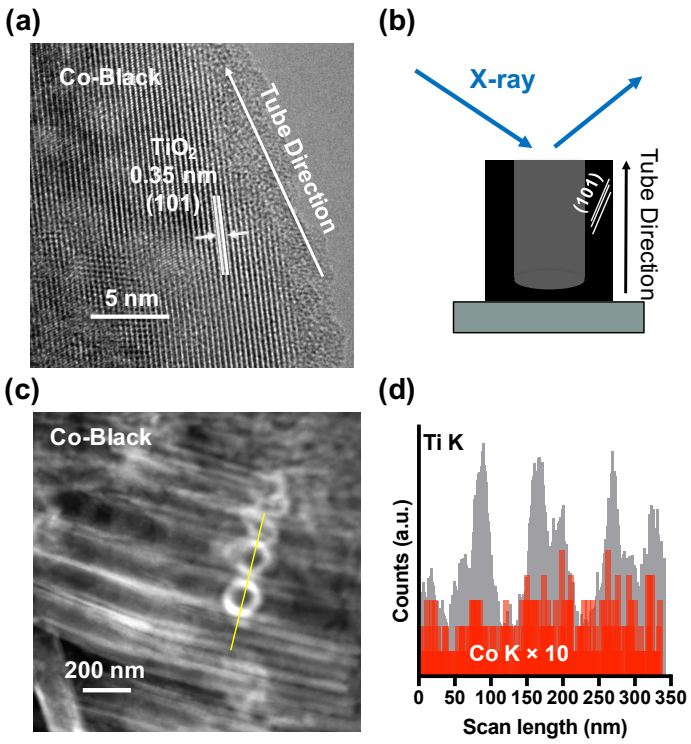

Figure S5. a) TEM image focusing on tube wall of Co-Black. b) Illustration of relative positions of the (101) plane, growth direction of nanotube, and incident X-ray in XRD analyses. c) Line scan of randomly selected broken nanotubes under HAADF-STEM mode. Yellow line shows the scan direction. d) Line scan signals as a function of scan length. The Co signal are enlarged ten times in Figure S4c for comparison with Ti signal.

Figure S5a shows the TEM image of the wall of a single Co-Black nanotube. The preferential exposure of the (101) plane is observed. The (101) plane is not strictly in parallel with tube growth direction. Therefore, as schematically shown in **Figure S5b**, there are chances that the incident X-ray is perpendicular to the (101) plane, resulting in the reflection of X-ray that can be detected by XRD. It is also reported that NTA's usually contain small anatase grains with random orientations.[10] Their (101) planes can be detected by XRD as well. With all above considered, the strongest (101) plane signal of Co-Black in the XRD analysis can be explained (**Figure S1**).

An EDS line-scan was performed at some randomly selected broken tubes under HAADF-STEM mode (**Figure S5c**). No particulate cobalt oxide was found. The variation of Co signal is roughly coherent with that of Ti signal (**Figure S5d**), indicating that Co ions were immobilized on the tube wall.

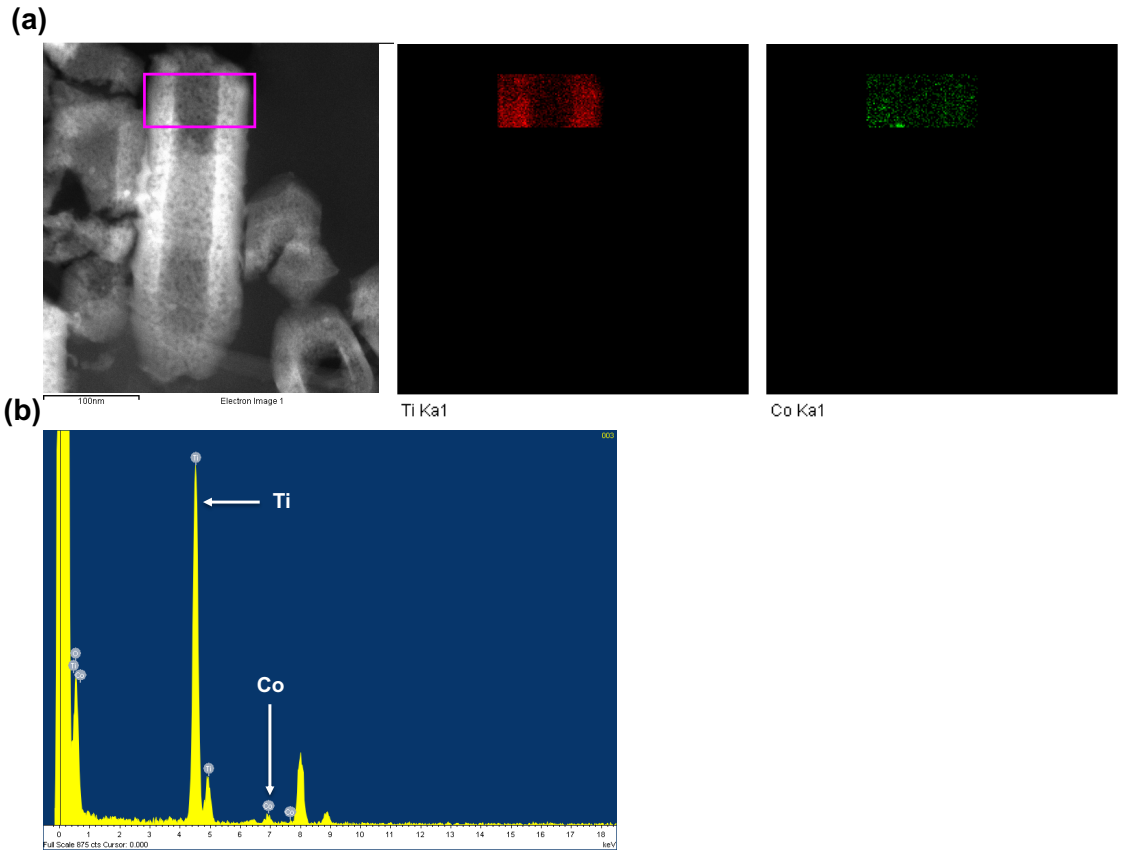

Figure S6. a) TEM-EDS mapping of Co-Black nanotube. b) EDS spectrum of selected area in Figure S6a. The atomic ratio of O: Ti: Co is quantified as 69.4: 30.0: 0.6.

The scattered dark dots on nanotube shown in **Figure S6a** represent the porous inner wall, which are also observed in previous study.[11] The EDS mapping clearly shows the well dispersion of Co element. No particulate CoO_x could be found.

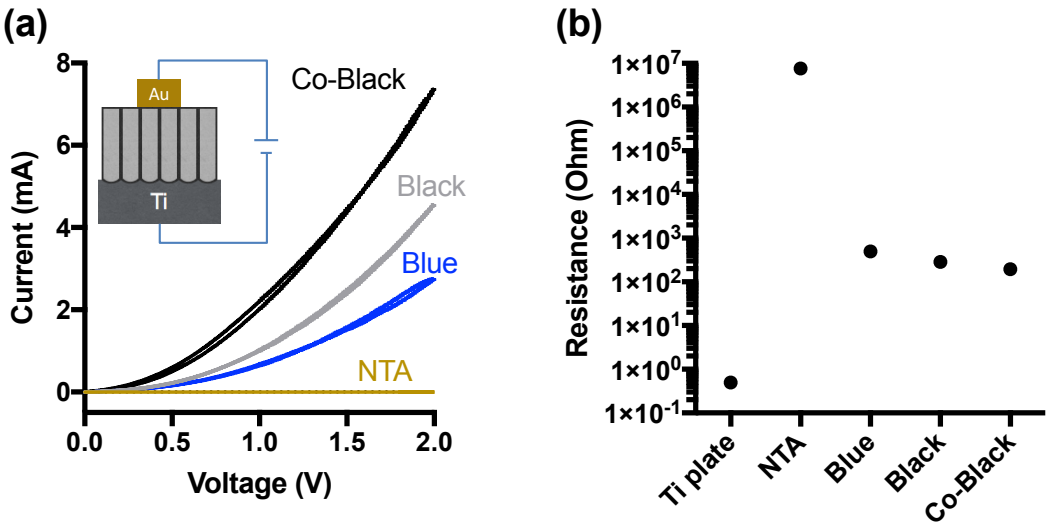

Figure S7. a) I–V characteristics of two-point solid-state measurements. b) Resistance of NTA electrodes.

The typical I-V characteristic of conductors should be a straight line. However, curves are found in the I-V functions of conductive NTA samples, indicating their semi-metallic properties.[12] Nevertheless, resistances were calculated from the force-zero regression line of I-V curves (R=V/I). Although these approaches may not yield entirely reliable values (in absolute terms), the results are still useful for the comparison of conductivity.

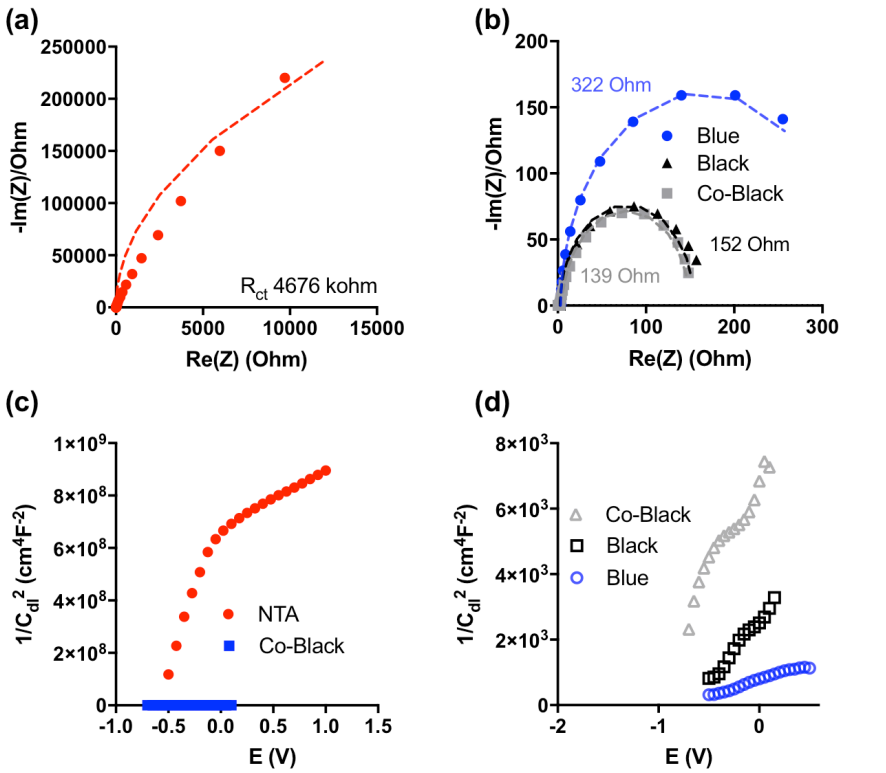

Figure S8. a & b) ElS spectra of NTA electrodes obtained at 0 V versus Pt wire reference electrode. Dash lines are the fitting results based on Randles circuit. c &d) Mott-Schottky plots of NTA electrodes.

The fitting of EIS spectra by Randles circuit gives the charge transfer resistance (R_{ct}) shown in **Figure S8 a and b**. The lower R_{ct} indicates a higher electrochemical activity towards Faradaic reactions. More than ten times reduction of R_{ct} was observed on blue, black and Co-Black NTA, implying the significant improvement of conductivity at the electrode/electrolyte interface.

Mott-Schottky plots illustrating the variation of C_{dl} as a function of potential are shown in **Figure S8 c and d**. The pristine NTA shows a clear capacitance-voltage dependence, evidencing the existence of space charge layer within n-type semiconductor. In contrast, such dependence is insignificant on conductive NTA electrodes. This means their capacitance is solely contributed by the Helmholtz layer at the solid-liquid interface. The elimination of the space charge layer at the electrode side suggests that conductive NTA electrodes have semi-metallic properties.

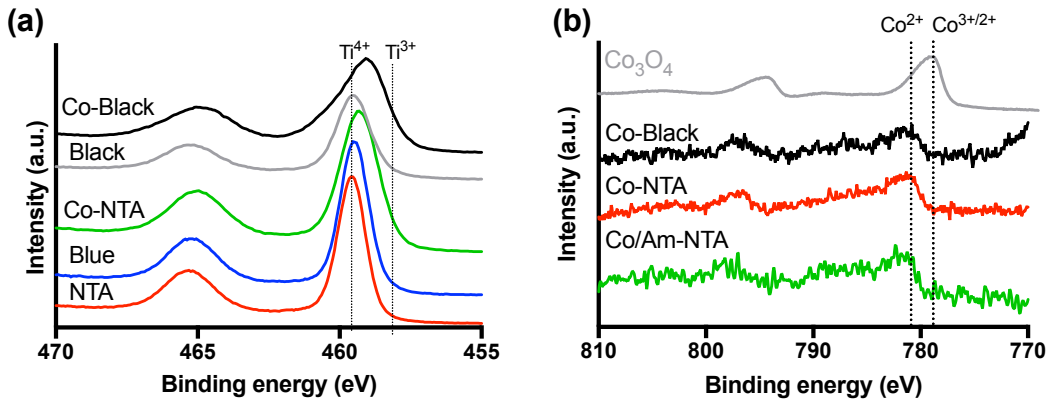

Figure S9. XPS spectra of a) Ti 2p and b) Co 2p orbitals.

The Ti $2P_{3/2}$ peak of NTA has a binding energy of 458.9 eV, highlighting its Ti^{4+} character.[13] Cathodization (blue NTA) and hydrogen reduction (black NTA) render insignificant change of Ti state. This is probably due to a large fraction of surficial Ti^{3+} sites that can be readily oxidized in ambient air. It is found that Co doping reduces the Ti oxidation state on Co-NTA. Even lower Ti oxidation states were observed on Co-Black.

$Co(NO_3)_2$ was loaded on Am-NTA via dip coating. The peak of Co $2p_{3/2}$ orbital of Co/Am-NTA located at 781 eV. This value can be used as a reference for Co^{2+} state. The thermal decomposition of $Co(NO_3)_2$ in air at 450 °C produced Co_3O_4, of which Co $2p3_{/2}$ orbital located at 780 eV, indicating the mixed +3/+2 states.[14] Annealing Co/Am-NTA in air and 5% H_2/Ar produced Co-NTA and Co-Black NTA respectively. Interestingly, Co species on these samples remained in 2+.

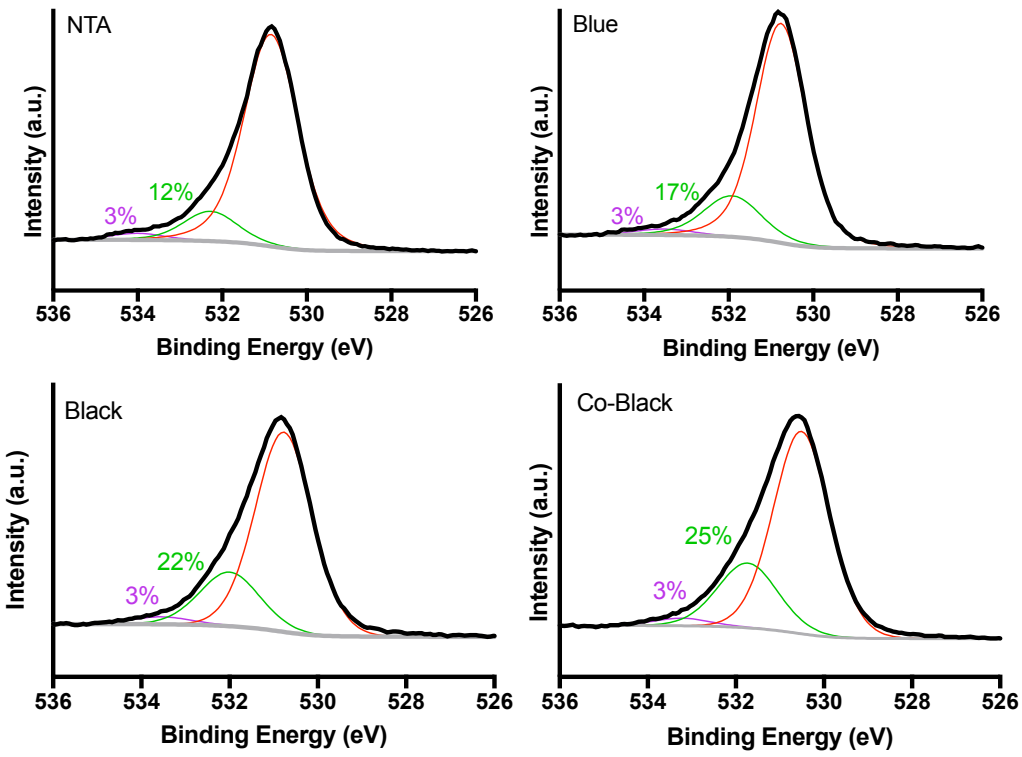

Figure S10. Deconvolution analyses of O 1s XPS spectra.

Peaks centered at 530-531 eV and 532-533 eV can be assign to lattice oxygen and hydroxyl group, respectively.[15-16] Peak located at 531 eV is assigned to adsorbed oxygen (O_2^{2-} or O^-),[17-18] which are originated from the dissociative adsorption of molecular oxygen on surficial O_v.[19] The filling of O_v by adsorbed oxygen could result in the oxidation of neighbor Ti^{3+}, which explain the lack of a strong Ti^{3+} signal in **Figure S9**. More importantly, the adsorbed oxygen could serve as an indirect measurement of native O_v. Via peak deconvolution, it is found that the relative concentrations of surficial O_v of Co-black (25%), black (22%) and blue (17%) NTA are higher than that of pristine NTA (12%).

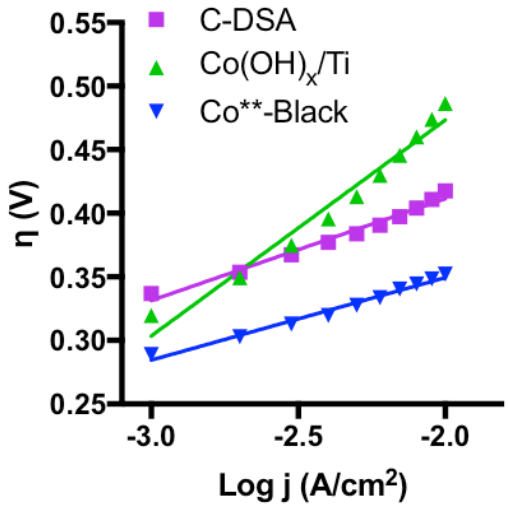

Figure S11. The comparison of Tafel Plots of C-DSA, Co(OH)x/Ti, and Co**-Black electrodes in 1 M KOH electrolyte.

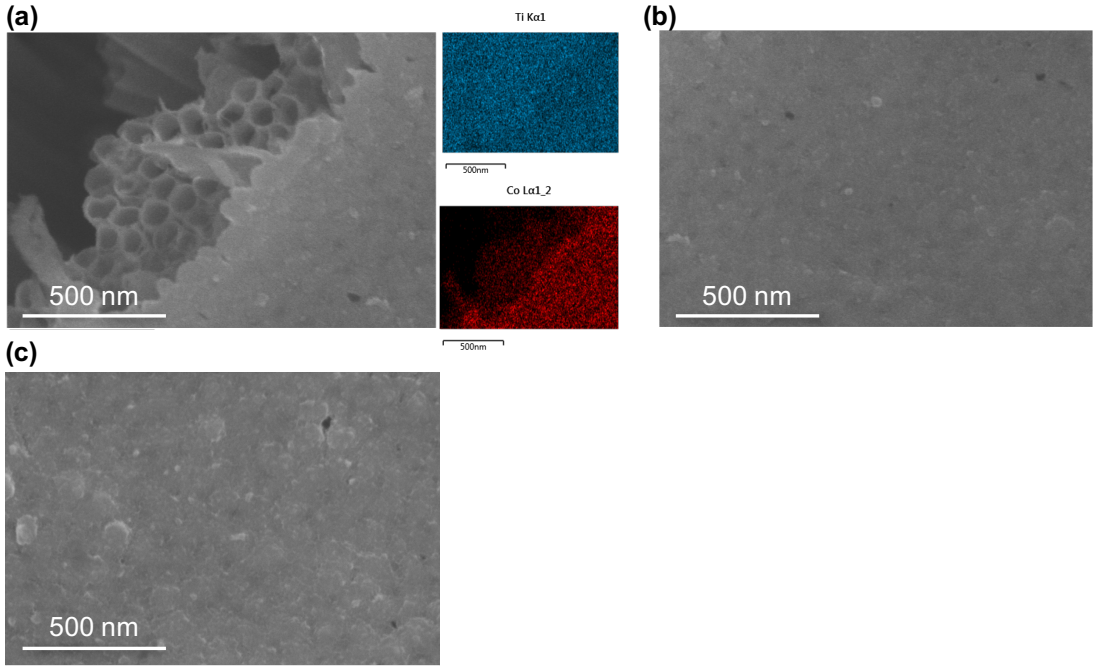

Figure S12. SEM-EDS image of a) defective and b) flawless area of Co*-Black NTA electrode. The defective area was created by scratching the Co*-Black electrode with scalpel blade. The underneath Co-Black substrate is exposed. c) SEM image of Co**-Black. Increasing the Co loading from 2.1 μm cm^{-2} for Co*-Black to 4.2 μm cm^{-2} for Co**-Black does not change the morphology of the top CoO_x film.

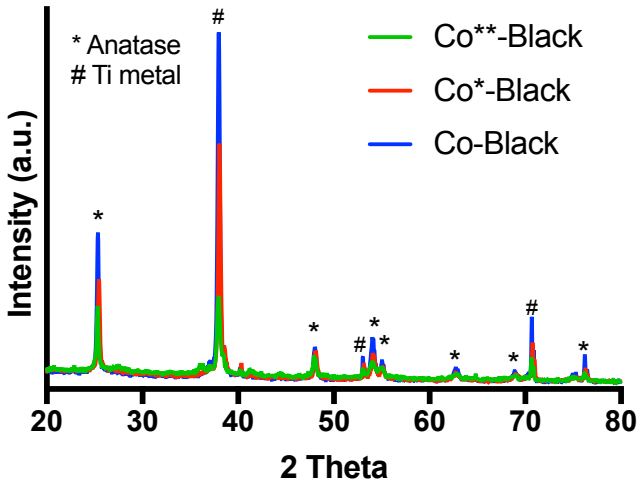

Figure S13. XRD of Co-Black, Co*-Black, and Co**-Black electrodes. The overall peak intensity of Co*- and Co**-Black is lower than that of Co-Black due to the surface coverage of CoO_x film. No peak other than that of Ti metal and anatase can be found on Co*-Black and Co**-Black, indicating that the atop CoO_x film is amorphous.

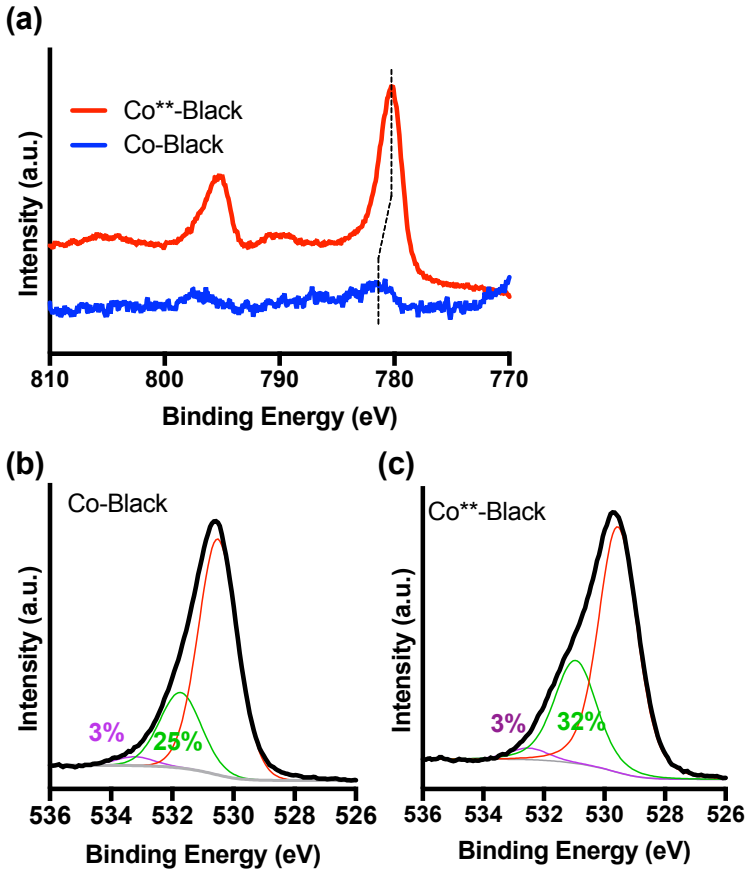

Figure S14. XPS spectra of a) Co 2p and b-c) O1s orbitals.

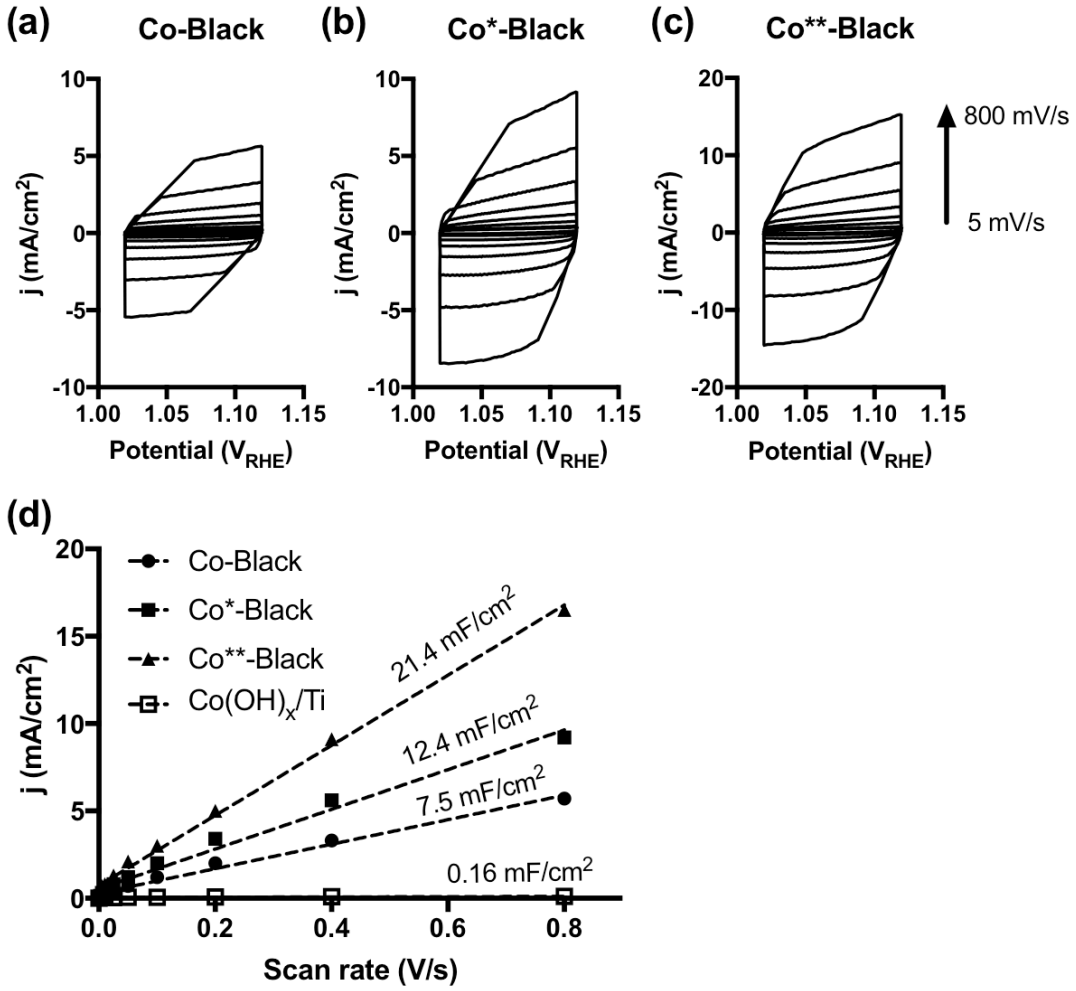

Figure S15. a-c) Cyclic voltammograms at 8 different scan rates: 5, 10, 25, 50, 100, 200, 400, and 800 mV s^{-1}. d) Capacitive currents as a function of scan rate.

The electrochemically active surface area of electrode was estimated by measuring the double-layer capacitance (C_{dl}). **Figure S15d** shows the capacitive currents as a function of scan rate. The slop of each line gives the C_{dl}.[20]

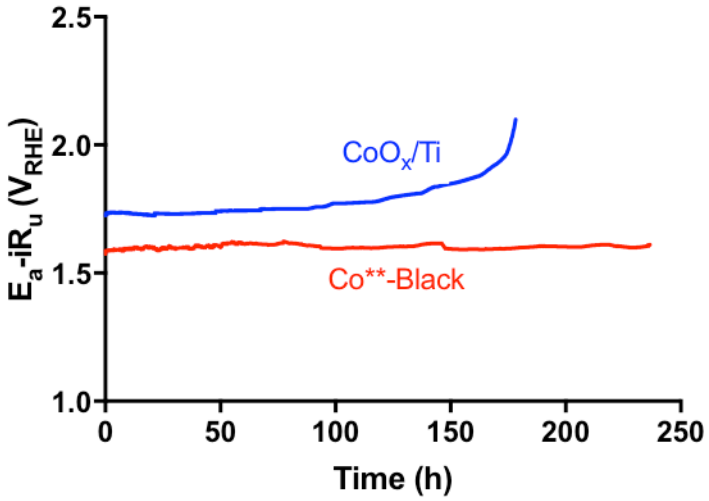

Figure S16. Anodic stability of CoO_x/Ti and Co**-Black electrodes in 1 M KOH at 10 mA cm^{-2}**.** The CoO_x/Ti electrode gradually deactivates as indicated by the increase of anodic potential. Co**-Black shows no sign of deactivation over the timeframe investigated.

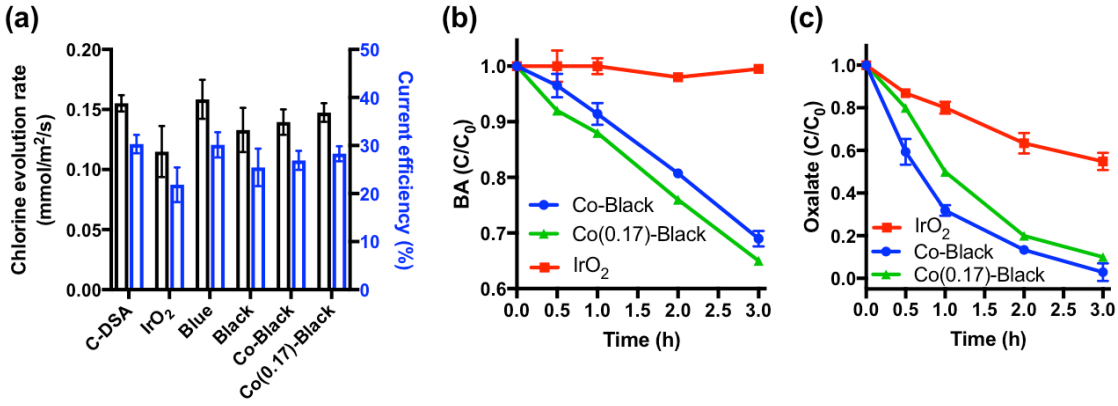

Figure S17. a) Chlorine evolution activity in 30 mM NaCl. b) hydroxyl radical production measured by electrochemical oxidation of benzoic acid. c) direct oxidation efficiency measured by electrochemical oxidation of oxalate ion. A constant current of 10 mA cm^{-2} was employed in the above tests.

Hydroxyl radical can be generated during water electrolysis. **Figure 2c** indicates that the anodic potentials reach 2.4-2.7 V_{RHE} which is considered as a thermodynamic criterion for ·OH generation.[21] Benzoic acid (BA) was selected as a radical probe compound ($r_{\cdot OH} = 5.90 \times 10^9$ M^{-1} s^{-1}). Faster degradation kinetics observed on Co-Black compared to IrO_2 indicates Co-Black has a higher activity toward ·OH generation than IrO_2 (**Figure S17b**). The direct electron transfer (DET) mechanism can also contribute to the oxidation of organic compounds. Oxalate ion selected to investigate the DET activity, as it is known to reactive via DET due to surface complex formation, but at the same time, oxalate reacts slowly with ·OH ($r_{\cdot OH} = 1.4 \times 10^6$ M^{-1} s^{-1}) compared to typical hydroxyl radical second-order rate constants.[22-23] **Figure S17c** indicates that Co-Black also shows higher DET activity than the corresponding IrO_2 electrode.

Co(0.17)-Black NTA electrode shows comparable activity with Co-Black NTA with regard to chlorine evolution, radical production, and DET reaction. Thus only Co-Black is subjected to the following test of wastewater treatment.

Table S1. Parameters and OER performance of electrocatalysts.

Catalyst	**Substrate/ cocatalyst[a]**	**Electrolyte**	**ECSA[b] (cm^2)**	**RF[c]**	**η at 1 mA/cm^2 (mV)**	**η at 10 mA/cm^2 (mV)**	**Ref.**
CoO_x	Black NTA	1 M KOH	3210	535	289	352	This study
$Co(OH)_x$	Ti	1 M KOH	4	4.1	319	480	This study
$Co(OH)_x$	GC	1 M KOH		10		400	[20]
CoO_x	Graphene	0.1 M KOH				294	[24]
$Co@Co_3O_4$	NC	1 M KOH				420	[25]
Spinel Co_3O_4	FTO	1 M KOH				390	[26]
Co_xO_y	NC	0.1 M KOH				430	[27]
CoO_x LDH	GC	1 M KOH				393	[28]
Co_3O_4 nanosheet	GC	1 M KOH				390	[29]
Co_3O_4 NW	GC	1 M KOH			320		[30]

[a] NC: nitrogen-doped carbon; GC: glassy carbon.

[b] Electrochemical surface area.

[c] Roughness factor (RF) = ECSA/geometric area.

The ECSA of Co**-Black NTA and Co(OH)x/Ti electrodes prepared in this study is calculated by

$$\mathrm{ECSA} = (C_{dl} \times A)/C_s$$

Where the double layer capacitance C_{dl} is obtained from **Figure S15**; A is the geometric area of electrode (6 cm^2); the specific capacitance of C_s = 0.04 mF cm^{-2} is reported by McCrory et al.[20]

References:

1. Dudarev, S. L.; Botton, G. A.; Savrasov, S. Y.; Humphreys, C. J.; Sutton, A. P., Electron-Energy-Loss Spectra and The Structural Stability of Nickel Oxide: An LSDA+U Study. *Phys. Rev. B* 1998, 57, 1505-1509.
2. Kresse, G.; Hafner, J., *Ab Initio* Molecular Dynamics for Liquid Metals. *Phys. Rev. B* 1993, 47, 558-561.
3. Kresse, G.; Furthmüller, J., Efficient Iterative Schemes for *Ab Initio* Total-Energy Calculations Using A Plane-Wave Basis Set. *Phys. Rev. B* 1996, 54, 11169-11186.
4. Kresse, G.; Joubert, D., From Ultrasoft Pseudopotentials to The Projector Augmented-Wave Method. *Phys. Rev. B* 1999, 59, 1758-1775.
5. Blöchl, P. E., Projector Augmented-Wave Method. *Phys. Rev. B* 1994, 50, 17953-17979.
6. Perdew, J. P.; Burke, K.; Ernzerhof, M., Generalized Gradient Approximation Made Simple. *Phys. Rev. Lett.* 1996, 77, 3865-3868.
7. Monkhorst, H. J.; Pack, J. D., Special Points for Brillouin-Zone Integrations. *Phys. Rev. B* 1976, 13, 5188-5192.
8. Aschauer, U.; Selloni, A., Hydrogen Interaction With The Anatase TiO_2(101) Surface. *Phys. Chem. Chem. Phys.* 2012, 14, 16595-16602.
9. Wang, L.; Maxisch, T.; Ceder, G., Oxidation Energies of Transition Metal Oxides within The GGA + U Framework. *Phys. Rev. B* 2006, 73, 195107.
10. Lee, K.; Mazare, A.; Schmuki, P., One-Dimensional Titanium Dioxide Nanomaterials: Nanotubes. *Chem. Rev.* 2014, 114, 9385-9454.
11. Gao, Z.-D.; Zhu, X.; Li, Y.-H.; Zhou, X.; Song, Y.-Y.; Schmuki, P., Carbon Cladded TiO_2 Nanotubes: Fabrication and Use in 3D-RuO_2 Based Supercapacitors. *Chem. Commun.* 2015, 51, 7614-7617.
12. Hahn, R.; Schmidt-Stein, F.; Salonen, J.; Thiemann, S.; Song, Y.; Kunze, J.; Lehto, V. P.; Schmuki, P., Semimetallic TiO_2 Nanotubes. *Angew. Chem. Int. Ed.* 2009, 48, 7236-7239.
13. Chen, X.; Liu, L.; Peter, Y. Y.; Mao, S. S., Increasing Solar Absorption for Photocatalysis with Black Hydrogenated Titanium Dioxide Nanocrystals. *Science* 2011, 331, 746-750.

14. Liang, Y.; Li, Y.; Wang, H.; Zhou, J.; Wang, J.; Regier, T.; Dai, H., Co_3O_4 Nanocrystals on Graphene as A Synergistic Catalyst for Oxygen Reduction Reaction. *Nat. Mater.* 2011, 10, 780-786.
15. Zhuang, L.; Ge, L.; Yang, Y.; Li, M.; Jia, Y.; Yao, X.; Zhu, Z., Ultrathin Iron-Cobalt Oxide Nanosheets with Abundant Oxygen Vacancies for the Oxygen Evolution Reaction. *Adv. Mater.* 2017, 29, 1606793.
16. Yang, Y.; Zhang, S.; Wang, S.; Zhang, K.; Wang, H.; Huang, J.; Deng, S.; Wang, B.; Wang, Y.; Yu, G., Ball Milling Synthesized MnO_x as Highly Active Catalyst for Gaseous POPs Removal: Significance of Mechanochemically Induced Oxygen Vacancies. *Environ. Sci. Technol.* 2015, 49, 4473-4480.
17. Yu, Z.; Gao, L.; Yuan, S.; Wu, Y., Solid Defect Structure and Catalytic Activity of Perovskite-Type Catalysts $La_{1-x}Sr_xNiO_{3-\lambda}$ And $La_{1-1.333x}Th_xNiO_{3-\lambda}$. *J. Chem. Soc., Faraday Trans.* 1992, 88, 3245-3249.
18. Kharas, K. C.; Lunsford, J. H., Catalytic Partial Oxidation of Methane over Barium Metaplumbate $BaPbO_3$: Possible Involvement of Peroxide Ion. *J. Am. Chem. Soc.* 1989, 111, 2336-2337.
19. Lu, G.; Linsebigler, A.; Yates Jr, J. T., The Adsorption and Photodesorption of Oxygen on the TiO_2 (110) Surface. *J. Chem. Phys.* 1995, 102, 4657-4662.
20. McCrory, C. C.; Jung, S.; Peters, J. C.; Jaramillo, T. F., Benchmarking Heterogeneous Electrocatalysts for the Oxygen Evolution Reaction. *J. Am. Chem. Soc.* 2013, 135, 16977-16987.
21. Siahrostami, S.; Li, G.-L.; Viswanathan, V.; Nørskov, J. K., One-or Two-Electron Water Oxidation, Hydroxyl Radical, or H_2O_2 Evolution. *J. Phys. Chem. Lett.* 2017, 8, 1157-1160.
22. Buxton, G. V.; Greenstock, C. L.; Helman, W. P.; Ross, A. B., Critical Review of Rate Constants for Reactions of Hydrated Electrons, Hydrogen Atoms and Hydroxyl Radicals (·OH/·O-) in Aqueous Solution. *J. Phys. Chem. Ref. Data* 1988, 17, 513-886.
23. Zaky, A. M.; Chaplin, B. P., Porous Substoichiometric TiO_2 Anodes as Reactive Electrochemical Membranes for Water Treatment. *Environ. Sci. Technol.* 2013, 47, 6554-6563.
24. Tong, Y.; Chen, P.; Zhou, T.; Xu, K.; Chu, W.; Wu, C.; Xie, Y., A Bifunctional Hybrid Electrocatalyst for Oxygen Reduction and Evolution: Cobalt Oxide

Nanoparticles Strongly Coupled to B, N-Decorated Graphene. *Angew. Chem. Inter. Ed.* 2017, 56, 7121-7125.

25. Aijaz, A.; Masa, J.; Rösler, C.; Xia, W.; Weide, P.; Botz, A. J.; Fischer, R. A.; Schuhmann, W.; Muhler, M., Co@ Co3O4 Encapsulated in Carbon Nanotube-Grafted Nitrogen-Doped Carbon Polyhedra as an Advanced Bifunctional Oxygen Electrode. *Angew. Chem. Inter. Ed.* 2016, 55, 4087-4091.
26. Wang, H.-Y.; Hung, S.-F.; Chen, H.-Y.; Chan, T.-S.; Chen, H. M.; Liu, B., In Operando Identification of Geometrical-Site-Dependent Water Oxidation Activity of Spinel Co_3O_4. *J. Am. Chem. Soc.* 2016, 138, 36-39.
27. Masa, J.; Xia, W.; Sinev, I.; Zhao, A.; Sun, Z.; Grützke, S.; Weide, P.; Muhler, M.; Schuhmann, W., Mn_xO_y/NC and Co_xO_y/NC Nanoparticles Embedded in a Nitrogen-Doped Carbon Matrix for High-Performance Bifunctional Oxygen Electrodes. *Angew. Chem. Inter. Ed.* 2014, 53, 8508-8512.
28. Song, F.; Hu, X., Exfoliation of Layered Double Hydroxides for Enhanced Oxygen Evolution Catalysis. *Nat. Commun.* 2014, 5, 4477.
29. Bao, J.; Zhang, X.; Fan, B.; Zhang, J.; Zhou, M.; Yang, W.; Hu, X.; Wang, H.; Pan, B.; Xie, Y., Ultrathin Spinel-Structured Nanosheets Rich in Oxygen Deficiencies for Enhanced Electrocatalytic Water Oxidation. *Angew. Chem.* 2015, 127, 7507-7512.
30. Wang, Y.; Zhou, T.; Jiang, K.; Da, P.; Peng, Z.; Tang, J.; Kong, B.; Cai, W. B.; Yang, Z.; Zheng, G., Reduced Mesoporous Co_3O_4 Nanowires as Efficient Water Oxidation Electrocatalysts and Supercapacitor Electrodes. *Adv. Energy Mater.* 2014, 4, 1400696.